RA-A73L62

Copy 43
RM SL55D14

NACA

NASA Class Change Notices,
Issue no. 4, Aug. 1, 1963

RESEARCH MEMORANDUM

Declassified
June 12, 1963

for the

Bureau of Aeronautics, Department of the Navy

N-R-10-11-63

STABILITY AND DRAG CHARACTERISTICS OF 1/10-SCALE MODEL

OF THE CONVAIR XF2Y-1 AIRPLANE WITH OPEN INLETS

CONTAINING BOUNDARY-LAYER SPLITTER PLATES AS

OBTAINED IN FREE FLIGHT AT MACH NUMBERS

BETWEEN 0.7 AND 1.5

TED No. NACA DE 365

By William M. Bland, Jr.

Langley Aeronautical Laboratory
Langley Field, Va.

NATIONAL ADVISORY COMMITTEE
FOR AERONAUTICS
WASHINGTON

NATIONAL ADVISORY COMMITTEE FOR AERONAUTICS

RESEARCH MEMORANDUM

for the

Bureau of Aeronautics, Department of the Navy

STABILITY AND DRAG CHARACTERISTICS OF 1/10-SCALE MODEL

OF THE CONVAIR XF2Y-1 AIRPLANE WITH OPEN INLETS

CONTAINING BOUNDARY-LAYER SPLITTER PLATES AS

OBTAINED IN FREE FLIGHT AT MACH NUMBERS

BETWEEN 0.7 AND 1.5

TED No. NACA DE 365

By William M. Bland, Jr.

SUMMARY

A 1/10-scale rocket-propelled model of the Convair XF2Y-1 water-based fighter airplane has been tested in free flight by the Langley Pilotless Aircraft Research Division in the Mach number range between 0.7 and approximately 1.5. The model had open inlets containing boundary-layer splitter plates to simulate the inlet arrangement of the full-scale airplane. The center of gravity was located 19.52 percent of the mean aerodynamic chord behind the leading edge of this chord.

Data obtained during the flight test indicated that, in general, the lift-curve slopes, the static-longitudinal-stability derivatives, the aerodynamic-center locations, and the combined damping-in-pitch derivatives agreed with the results obtained from the flight test of another open-inlet model without boundary-layer splitter plates except near Mach number 0.91 where some difference was noted in lift-curve slope and the damping-in-pitch derivatives. The lateral data indicated static stability and dynamic stability with low damping throughout the Mach number range. The mass-flow ratio was increased throughout the Mach number range investigated and the pressure recovery aft of the inlet was increased except at transonic speeds by installing boundary-layer splitter plates in the inlets.

INTRODUCTION

The fourth and final model in a series of 1/10-scale rocket-propelled models of the Convair XF2Y-1 water-based fighter airplane has been flight-tested at high subsonic, transonic, and supersonic speeds by the Langley Pilotless Aircraft Research Division as requested by the Bureau of Aeronautics, Department of the Navy. This model, unlike the previous three (which are reported in refs. 1 to 3), was modified to make the inlets similar to those on the full-scale airplane so that some measure of inlet performance could be made. Drag, longitudinal-stability, and lateral-stability measurements were also made during the flight test.

The results of this flight test, which was conducted at the Langley Pilotless Aircraft Research Station, Wallops Island, Va., are presented for the Mach number range between 0.7 and 1.5 corresponding to a Reynolds number range between approximately 8.6×10^6 and approximately 21.2×10^6.

SYMBOLS

A_D cross-sectional area of each inlet and duct in plane perpendicular to plane of symmetry, sq in.

A_e cross-sectional area at exit, sq in.

A_{equiv} cross-sectional area of equivalent body, sq ft

A_i cross-sectional area at inlet, sq in.

b   wing span, ft

$\bar{c}$ wing mean aerodynamic chord, ft

D_{max} maximum diameter of equivalent body of revolution, ft

l body length, ft

r_{equiv} radius of equivalent body of revolution, ft

S   total included wing area, sq ft

X   distance from nose, ft

X_{ac} aerodynamic-center location, $X_{cg} - 100 \dfrac{C_{m_\alpha}}{C_{L_\alpha}}$, percent $\bar{c}$

X_{cg} nondimensional center-of-gravity location, percent $\bar{c}$

y axis passing through center of gravity, normal to plane of symmetry, zero on plane of symmetry

M Mach number

m mass flow, slugs/sec

q_0 free-stream dynamic pressure, lb/sq ft

R Reynolds number, based on $\bar{c}$

V velocity, ft/sec

γ ratio of specific heats, 1.4

α angle of attack, deg

$\dot{\alpha}$ rate of change of angle of attack with time, $\dfrac{d\alpha}{dt}\dfrac{1}{57.3}$

β angle of sideslip, deg

θ angle of pitch, deg

q rate of change of angle of pitch with time, $\dfrac{d\theta}{dt}\dfrac{1}{57.3}$

t time, sec

H total pressure, lb/sq in.

p static pressure, lb/sq in.

P pressure coefficient, $\dfrac{p - p_0}{q_0}$

C_C chord-force coefficient, $\dfrac{\text{Chord force}}{q_0 S}$

C_D drag coefficient, $\dfrac{\text{Drag}}{q_0 S}$

C_L lift coefficient, $\dfrac{\text{Lift}}{q_o S}$

C_m pitching-moment coefficient, $\dfrac{\text{Pitching moment}}{q_o S \bar{c}}$

C_n yawing-moment coefficient, $\dfrac{\text{Yawing moment}}{q_o S b}$

C_N normal-force coefficient, $\dfrac{\text{Normal force}}{q_o S}$

C_Y side-force coefficient, $\dfrac{\text{Side force}}{q_o S}$

$C_{L\alpha}$ lift-curve slope, $\dfrac{dC_L}{d\alpha}$

$C_{m\alpha}$ static-longitudinal-stability derivative, $\dfrac{dC_m}{d\alpha}$

$C_{n\beta}$ static-directional-stability derivative, per deg

$C_{Y\beta}$ side-force-curve slope, $\dfrac{dC_Y}{d\beta}$

$C_{m_q} + C_{m_{\dot{\alpha}}}$ combined damping-in-pitch derivatives, per radian

$$C_{m_q} = \frac{dC_m}{d\left(\dfrac{q\bar{c}}{2V}\right)}$$

$$C_{m_{\dot{\alpha}}} = \frac{dC_m}{d\left(\dfrac{\dot{\alpha}\bar{c}}{2V}\right)}$$

Subscripts:

b   base

D   duct

e   exit

i   inlet

int   internal

o   free-stream condition

t   trim

MODEL DESCRIPTION

The general characteristics of the model are shown in the drawing in figure 1, in the photograph in figure 2, and in table I. The area distribution of the model and the profile of a body of revolution with an equivalent area distribution are shown in figure 3.

The fuselage shell was made of plastic and fiber-glass laminate. The wings were constructed of laminated wood with aluminum-alloy chord-plane stiffeners and inlays under the wing surface. Construction of the vertical tail was similar except that 0.032-inch Inconel plates were inlaid, in both sides, over a large portion of the tail, as can be seen in figure 2.

The elevons, which were full-span, were deflected 4.05°, trailing edge up, so the model would trim at a positive angle of attack. The rudder was not deflected.

Ducts, which in the full-size airplane house the turbojet engines and form the air induction and exhaust systems, were left open so that inlet conditions of the airplane would be simulated. The basic inlets on the model were originally the same as those used on the model reported in reference 2. However, these inlets were modified by adding boundary-layer splitter plates (fig. 4) of such size that the inlets became similar to the one described in reference 4 as the basic blunt inlet with 15° duct-ramp angle, which is the one used on the full-size airplane. General features and the cross-sectional area distribution of the inlets and ducts are shown in figures 4 and 5. To insure that duct exit velocities would not exceed $M = 1.0$, the cross-sectional area of each exit was made the same as the minimum inlet cross-sectional area by the

addition of choking plates as shown in figure 6. Boundary-layer air separated by the splitter plates was immediately returned to the free stream through slots located on the outside and top of each inlet as shown in figure 4.

Instruments were installed in the nose and in the fuselage below the wing in a manner similar to the instrument installation described in reference 1. The instruments, which were eleven in number, were used to measure angles of attack and sideslip, acceleration along each of the body axes, total pressure outside the model (fig. 1) and in the port duct, and static pressure inside the port duct and on the port base. Total pressure in the duct was measured by means of a slotted averaging rake (fig. 5(a)) that extended across the duct at the longitudinal station representing the location of the turbojet-engine compressor face on the full-scale airplane. Results of tests at the Lewis Flight Propulsion Laboratory, which are unpublished, indicate that the slotted averaging rake has measured pressure recoveries within a percent of observed total-pressure recovery. Static pressure in the port duct was measured just ahead of the total-pressure rake and near the exit by manifolding four evenly spaced orifices on the inside periphery of the duct at each measuring station (fig. 5(b)) to a single instrument. A similar method was used to measure the base pressure in the annular area around the port exit (fig. 6).

TEST PROCEDURE

The model and booster assembly were launched from a mobile-type launcher inclined at an angle of approximately 60° above the horizontal as shown in figure 7. After being accelerated to a Mach number of approximately 1.5 by the booster rocket motor, the model separated from the booster assembly and coasted in free flight, being decelerated by drag and its weight component along the flight path. During the period of coasting flight the model was disturbed in pitch by pulse rockets which were located at the rear of the model in the lower part of the fuselage.

During the flight of the model, information from each instrument contained within the model was transmitted continuously from the model to the ground receiving station where it was recorded. At the ground station a radar tracking unit was used to determine the position of the model in space throughout the flight. A radiosonde was used to measure atmospheric conditions at the time of the flight.

ACCURACY

Systematic errors in the various measured quantities due to inherent limitations in the measuring, recording, and data-reduction systems are

estimated to be within ±1 percent of full-scale instrument calibration which results in the following limits:

M	ΔC_N	ΔC_C	ΔC_Y	ΔH, lb/sq in.	Δp, lb/sq in.	$\Delta \alpha$ and $\Delta \beta$, deg
1.4	±0.002	±0.001	±0.001	±0.40	±0.10	±0.10
1.1	±.004	±.001	±.001	±.40	±.10	±.10
.8	±.008	±.002	±.002	±.40	±.10	±.10

However, the accuracy of other quantities, such as slopes, which were obtained by fairing through data points, is believed to be better than that implied by the accuracy of the individual quantities involved.

Systematic errors in Mach number, which was calculated from p_0 and H, are estimated to be within ±0.005 at the highest Mach number of the test and ±0.020 at the lowest Mach number.

RESULTS AND DISCUSSION

Presented in figure 8 is the variation of Reynolds number, based on the wing mean aerodynamic chord, with Mach number as obtained during this test.

A sample of the time histories of some of the basic quantities resulting from measurements made while the model was in coasting flight is shown in figure 9. Oscillations of some of these quantities indicate the behavior of the model as it recovered from disturbances. The earliest set of oscillations shown was caused by an abrupt change in trim that occurred as the model separated from the booster assembly. The other set of oscillations shown was obtained as the model recovered from a pulse-rocket disturbance. Other oscillations were obtained as a result of a later pulse-rocket disturbance.

Stability Characteristics

Longitudinal.- The lift coefficient was calculated from the basic quantities by the expression $C_L = C_N \cos \alpha + C_C \sin \alpha$. Also, since the model was equipped with two instruments for measuring normal accelerations, one in the nose and one aft of the center of gravity, it was

possible to determine the pitching acceleration and the total instanta-
neous pitching-moment coefficient. Typical variations of C_L and C_m
with α are shown in figures 10 and 11, respectively. Values of the
slopes C_{L_α} and C_{m_α}, as obtained by applying the least-squares method
to the complete range of data obtained during each of the first four
oscillations following a disturbance, are shown in figures 12(a) and 12(b),
respectively. Values of C_{m_α} were also calculated by applying the aver-
age period of each set of angle-of-attack oscillations to the one-degree-
of-freedom method of reference 5 and, as shown in figure 12(b), agree
very well with the values previously determined. Included in figures 12(a)
and 12(b) are values of C_{L_α} and C_{m_α} from reference 2 which show good
agreement with the results of the present test at supersonic speeds but
are somewhat higher in the subsonic region.

By using the values of C_{L_α} and C_{m_α} obtained during the present
test (figs. 12(a) and 12(b)), it was possible to compute the aerodynamic-
center locations shown in figure 12(c). The values show that the aero-
dynamic center moved rearward from approximately $0.40\bar{c}$ at $M \approx 0.91$ to
approximately $0.46\bar{c}$ as the Mach number increased to $M \approx 1.22$ and
$M \approx 1.45$. These locations of the aerodynamic center agree with those
from reference 2 which are also included in figure 12(c).

Further analysis of the angle-of-attack oscillations by a method
included in reference 5 resulted in the combined damping-in-pitch deriva-
tives presented in figure 12(d) for three Mach numbers. These deriva-
tives indicated for this model the low magnitude of pitch damping that
is characteristic of configurations without horizontal tail surfaces.
Compared with the damping-in-pitch derivatives from reference 2, the
results of the present test show good agreement at $M \approx 1.22$ and
$M \approx 1.49$ but not at $M \approx 0.91$. A large portion of the difference at
$M \approx 0.91$ is due to the difference previously noted in the values of C_{L_α}
at this Mach number (fig. 12(a)). The time to damp to half amplitude
used in the evaluation of $C_{m_q} + C_{m_{\dot{\alpha}}}$ for $M \approx 1.49$ was obtained for
only the first few angle-of-attack oscillations in that set. The later
oscillations, which had amplitudes of approximately $\pm 0.6^\circ$, were irregular
and less damped.

Lateral.- The time histories of the angle of sideslip and side-force
coefficient, portions of which are included in figure 9, showed oscilla-
tions that apparently resulted from a lateral component of the pitch
disturbances. Analyses of these oscillations indicated no dynamic lateral
instability at either subsonic or supersonic speeds; although the damping
of these oscillations was low.

Values of the static-directional-stability derivative as calculated by applying the average period of each set of angle-of-sideslip oscillations to the single-degree-of-freedom method, as was done in references 1 and 3, are as follows:

Mach number	C_{n_β}, per deg
1.37	0.0014
1.16	.0018

No attempt was made to calculate a value of C_{n_β} for the subsonic set of oscillations because the oscillations were very irregular in shape and period.

Typical variations of C_Y with β are shown in figure 13. Values of C_{Y_β}, which were calculated by applying the least-squares method to the complete range of data obtained during each of the first two or three oscillations following a disturbance, are presented in figure 14. It is shown in figure 14 that C_{Y_β} remained fairly constant at a value near -0.01 throughout the Mach number range investigated.

Trim Characteristics

The variations with Mach number of the trim angle of attack and the trim lift coefficient obtained during coasting flight are presented in figure 15. Similarly, the variations with Mach number of the trim angle of sideslip and the trim side-force coefficient are presented in figure 16. These lateral data show that the model did not trim at exactly 0° sideslip as might be expected for a configuration that is symmetrical about the $y = 0$ plane, probably because of some construction asymmetry.

An abrupt change in the magnitudes of β and C_Y, not associated with a pulse-rocket disturbance, occurred near $M \approx 0.96$ as can be seen in figure 16. By comparing figures 15 and 16 it can be noted that, as the model decelerated through the Mach number range, the abrupt change in lateral trim occurred at about the same time as the change in longitudinal trim began. Both the lateral change and accompanying small-magnitude oscillations in pitch were analyzed to obtain values of C_{Y_β} and C_{L_α} near $M \approx 0.96$ as shown in figures 14 and 12(a), respectively.

Drag Characteristics

The base pressure coefficient as obtained from measurements of the average pressure in the annular area around the port exit is presented in figure 17. The magnitude of the base pressure coefficient and the variation with Mach number (fig. 17) are very similar to the base-pressure-coefficient data presented in reference 2. By assuming that the base pressure measured on the annulus about the port exit was representative of the pressure on the annulus about the starboard exit and on the rear faces of the respective choking plates, it was possible to compute the magnitude of the base drag coefficient throughout the Mach number range, as shown in figure 18(a). Base-drag-coefficient data from reference 2, also included in figure 18(a), are lower than the results of the present test throughout the Mach number range. Not all the difference between the base-drag-coefficient curves is due to a difference in base pressure coefficient. Some of this difference between the curves (27 percent at $M = 0.7$, 100 percent at $M = 1.1$, and 57 percent of the difference at $M = 1.4$) is due to the difference in the base areas of the respective models.

By assuming that the flow through both ducts was the same, the internal-drag coefficient was calculated from the measurements made in the port duct by the expression

$$C_{D_{int}} = \frac{2\left[\gamma\left(\frac{m_D}{m_0} M_0{}^2 p_0 A_i - M_e{}^2 p_e A_e\right) - \left(p_e - p_0\right) A_e\right]}{q_0 S}$$

The variation of the internal-drag coefficient with Mach number obtained in the present test is shown in figure 18(b) with similar results from reference 2. The magnitudes of the internal-drag coefficients from both the present test and reference 2 are small when compared with the total drag coefficient.

The variation of the total drag coefficient with Mach number for the trim conditions of the present test is presented in figure 19. Values of the base drag coefficient and the internal-drag coefficient (fig. 18) were subtracted from the total drag coefficient to obtain the variation with Mach number of the net drag coefficient presented in figure 20. The net drag coefficient obtained from the present test is somewhat greater than that obtained from data of reference 2 (as shown in fig. 20), as might be expected since the model used in the present test had a larger elevon deflection and trimmed at a higher lift coefficient throughout most of the Mach number range.

Inlet and Duct Characteristics

The addition of boundary-layer splitter plates to the inlets of the model reported in reference 2 decreased the actual mass of air handled by the inlets per unit time, but the decrease was not in proportion to the decrease in inlet area thus indicating more efficient operation. The inlet area was decreased by 38 percent and the mass flow was only decreased by approximately 22 percent at $M = 0.7$, 33 percent at transonic speeds, and 29 percent near $M = 1.25$. In figure 21 it is shown that the mass-flow ratio as obtained for the inlets with boundary-layer splitter plates is greater throughout the Mach number range for which measurements were obtained than the mass-flow ratio obtained for the inlets without the splitter plates (ref. 2).

It is also shown in figure 21 that the total-pressure recovery at the duct station corresponding to the location of the turbojet-engine compressor face in the full-scale airplane was improved throughout most of the Mach number range. The region of greatest improvement occurred at the higher Mach numbers of the test where the measured recovery approached the theoretical total-pressure recovery across a normal shock wave (ref. 6).

CONCLUDING REMARKS

A 1/10-scale rocket-propelled model of the Convair XF2Y-1 airplane with open inlets has been flight-tested to a maximum Mach number of approximately 1.5. This model was similar to another open-inlet model tested previously with the exception that boundary-layer splitter plates were installed to make the inlets similar to those of the full-scale airplane. The center of gravity was located 19.52 percent of the mean aerodynamic chord behind the leading edge of the mean aerodynamic chord. Results of this test indicated that, in general, values of the lift-curve slope, the static-longitudinal-stability derivative, the aerodynamic-center location, and the combined damping-in-pitch derivatives agreed with the results obtained from the flight test of the model without boundary-layer splitter plates, except near a Mach number of approximately 0.91 where some differences were noted in lift-curve slope and damping-in-pitch derivatives. The lateral data indicated static stability and dynamic stability with low damping throughout the Mach number range.

The addition of boundary-layer splitter plates in the inlets increased the mass-flow ratio throughout the Mach number range and increased the pressure recovery behind the inlet except at transonic speeds.

Langley Aeronautical Laboratory,
    National Advisory Committee for Aeronautics,
        Langley Field, Va., March 24, 1955.

                                        William M. Bland, Jr.
Approved: Aeronautical Research Scientist
            Joseph A. Shortal
        Chief of Pilotless Aircraft Research Division

DY

<div align="center">REFERENCES</div>

1. Bland, William M., Jr., and Nelson, Robert L.: Results of a Power-On Flight of a 1/10-Scale Rocket-Propelled Model of the Convair XF2Y-1 Airplane at a Mach Number of 1.53 - TED No. NACA DE 365. NACA RM SL53I30a, Bur. Aero., 1953.

2. Welsh, Clement J., Bland, William M., Jr., and Walters, Richard E.: Rocket-Model Investigation of the Longitudinal Stability and Drag Characteristics of a 1/10-Scale Model of the Convair XF2Y-1 Airplane Having Open Ducts and the Elevons Deflected Upward 3.5° - TED No. NACA DE 365. NACA RM SL54A05, Bur. Aero., 1954.

3. Bland, William M., Jr.: Results of Free-Flight Test of 1/10-Scale Model of the Convair XF2Y-1 Airplane Between Mach Numbers of 0.7 and 1.45, Including Power-On Flight at Mach Number 1.2 - TED No. NACA DE 365. NACA RM SL54B05, Bur. Aero., 1954.

4. Thomas, D. M., and Meyer, R. A.: Y2-2 Airplane Configuration - Second Supersonic Test at M = 1.50 at OAL: Daingerfield Test 233-3. Memo A-2-3, Consolidated Vultee Aircraft Corp., Aug. 15, 1951.

5. Gillis, Clarence L., Peck, Robert F., and Vitale, A. James: Preliminary Results From a Free-Flight Investigation at Transonic and Supersonic Speeds of the Longitudinal Stability and Control Characteristics of an Airplane Configuration With a Thin Straight Wing of Aspect Ratio 3. NACA RM L9K25a, 1950.

6. The Staff of the Ames 1- by 3-Foot Supersonic Wind-Tunnel Section: Notes and Tables for Use in the Analysis of Supersonic Flow. NACA TN 1428, 1947.

TABLE I

GENERAL CHARACTERISTICS OF THE FOURTH 1/10-SCALE ROCKET-PROPELLED

MODEL OF THE CONVAIR XF2Y-1

Wing:
  Total included area, sq ft 5.63
  Span, ft 3.37
  Mean aerodynamic chord, ft 2.14
  Aspect ratio 2.03
  Airfoil section:
    At center line . . . . NACA 0002.89-65 (modified)
    From 86 percent of half-span to tip . . . NACA 0004-65 (modified)
Tail:
  Exposed area, sq ft 0.8
  Airfoil section:
    At root . . . . NACA 0003-65 (modified)
    At tip . . . . NACA 0004-65 (modified)
Elevon deflection, trailing edge up, deg 4.05
Weight, lb 93.6
Moment of inertia about body axis, slug-ft^2:
  Roll 0.38
  Yaw 6.01
  Pitch 5.57
Center-of-gravity positions:
  Longitudinal, percent M.A.C. 19.52
  Vertical, in. above reference line 0.61
Angle principal axis rotated below body axis at nose, deg 0.9
Area of annulus and choking plate of both exits, sq in. 6.78
Exit annular area, sq in.:
  Port 5.44
  Starboard 5.44
Exit diameter, in.:
  Port 1.73
  Starboard 1.74
Choking-plate thickness, in.:
  Port 0.19
  Starboard 0.17
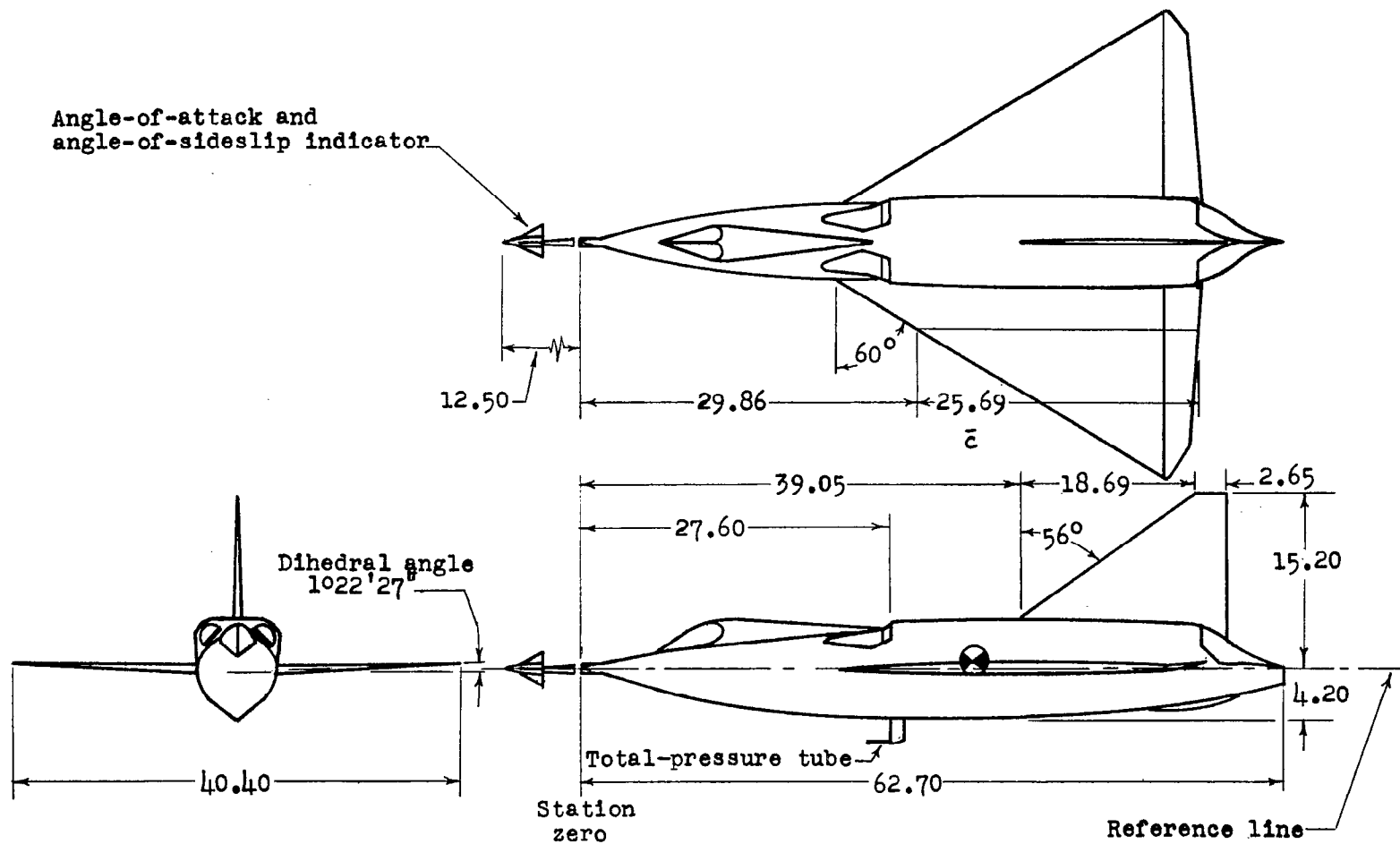
Figure 1.- General arrangement of model. All linear dimensions in inches.
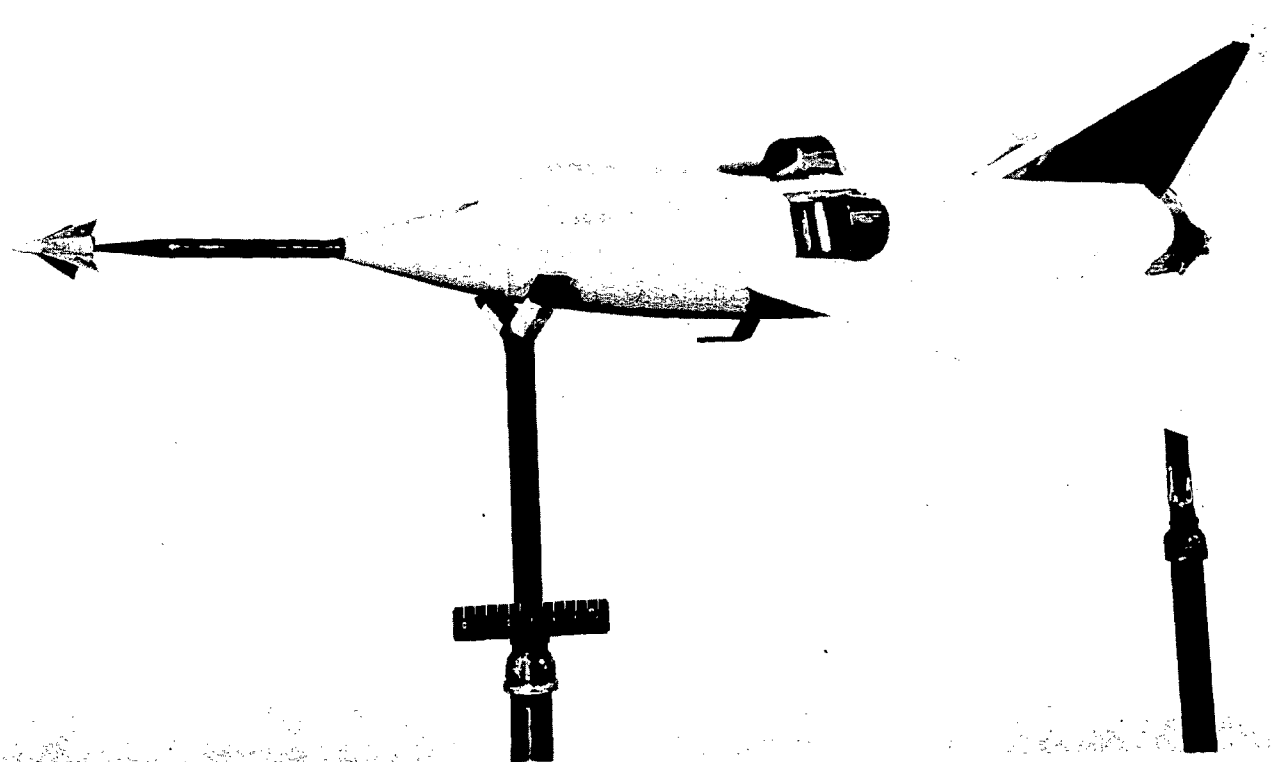
Figure 2.- External view of complete model.

L-83896.1
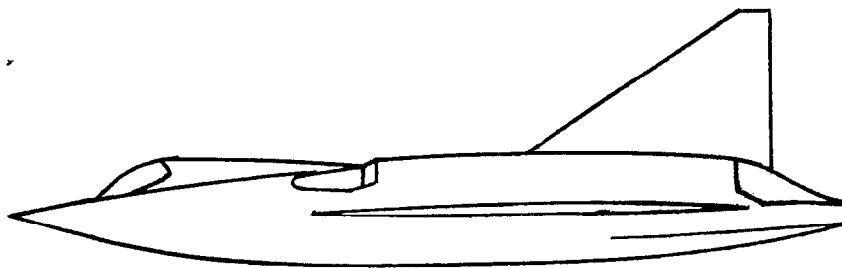
(a) Model.
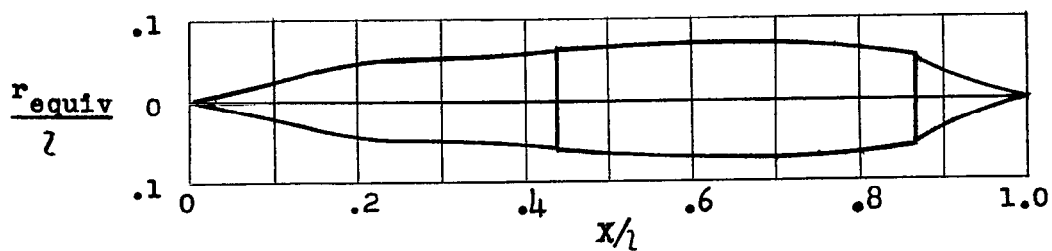
(b) Profile of body with circular cross sections equivalent in area to
model with mass-flow ratio of 0.75. $l/D_{max} = 7.12$.
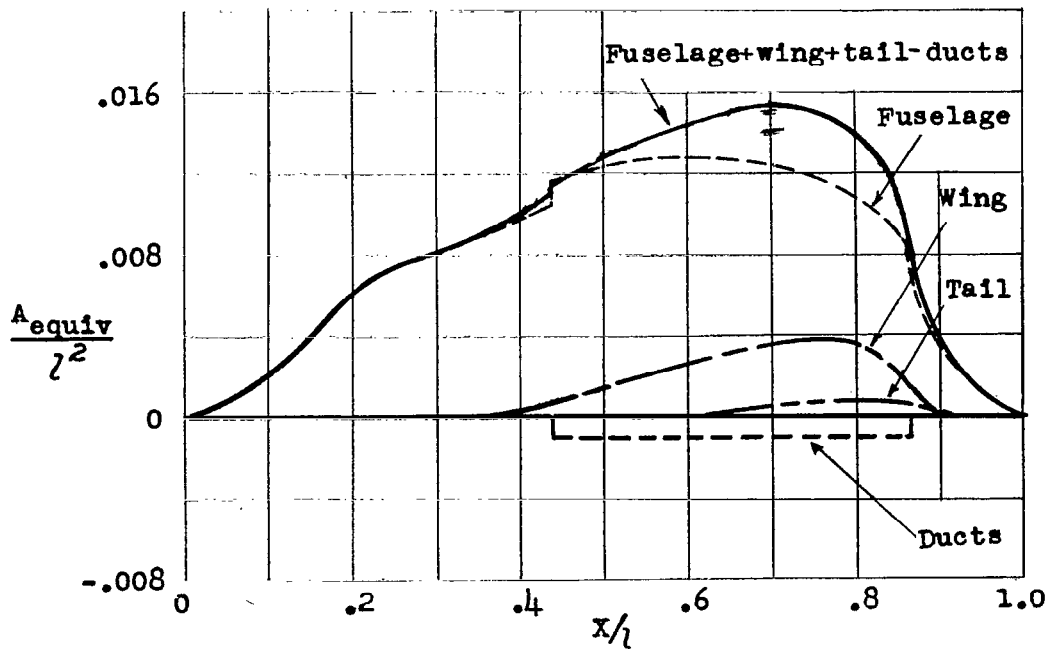
(c) Longitudinal distribution of cross-sectional area.

Figure 3.- Physical characteristics of the test configuration.

Boundary-layer
air exits

Port boundary-layer
splitter plate
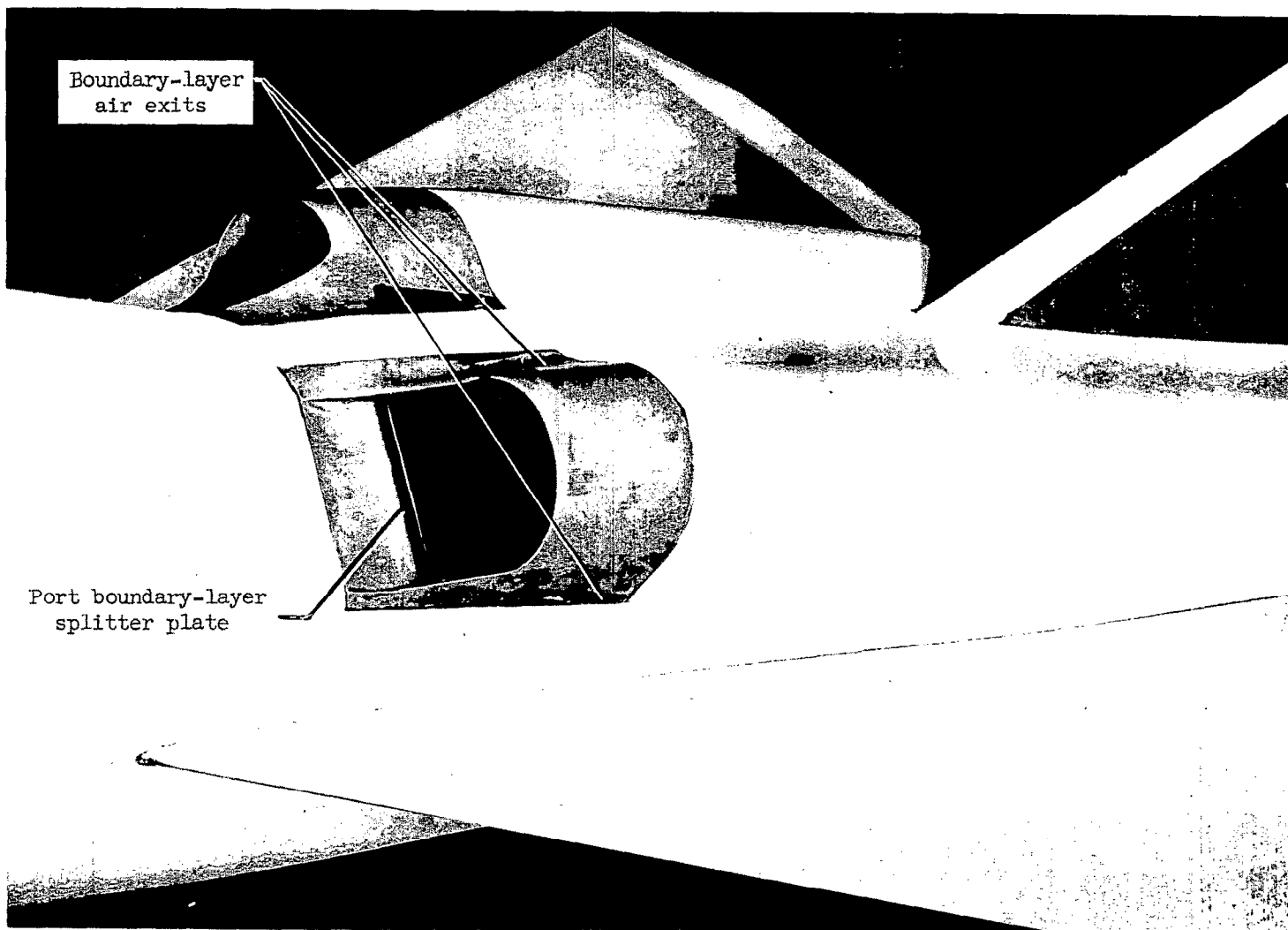
L-83895.1

Figure 4.- Closeup of inlets showing splitter plates and boundary-layer
air exits.
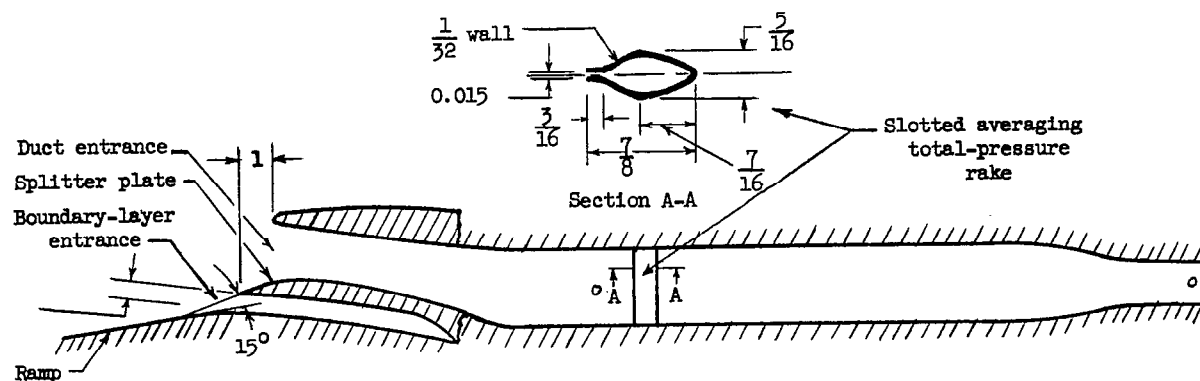
(a) Basic blunt-lip inlet with 15° duct-ramp angle, duct, and slotted averaging total-pressure rake. All linear dimensions in inches.
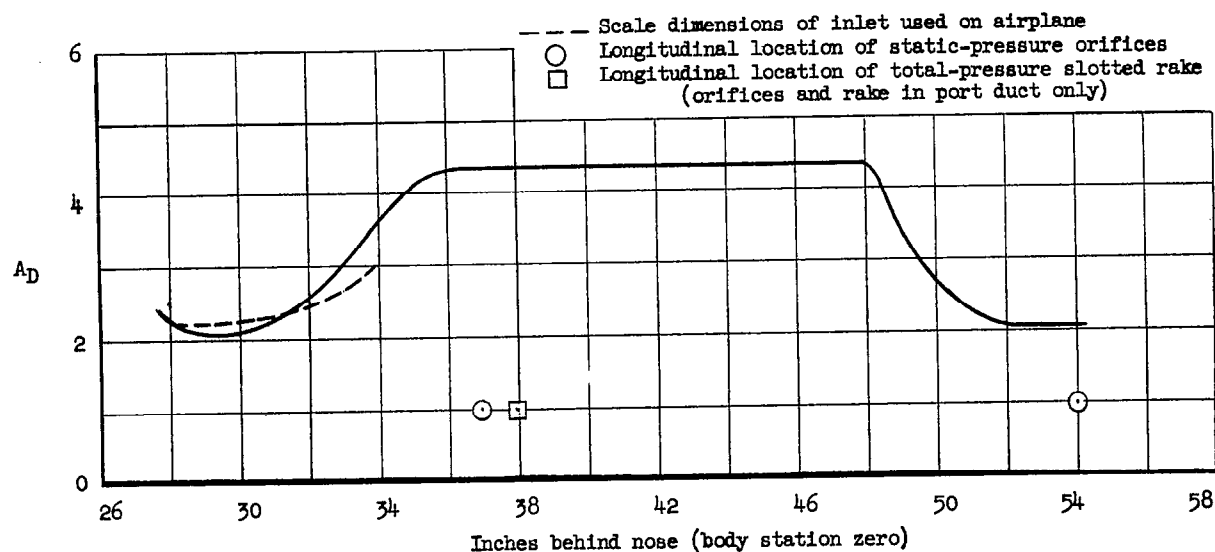
(b) Variation of cross-sectional area of inlet and duct with longitudinal distance.

Figure 5.- Geometric characteristics of inlets and ducts.

Base static-pressure orifices
manifolded together
(station 54.34)

Four exit static-pressure
orifices manifolded together
(station 54)
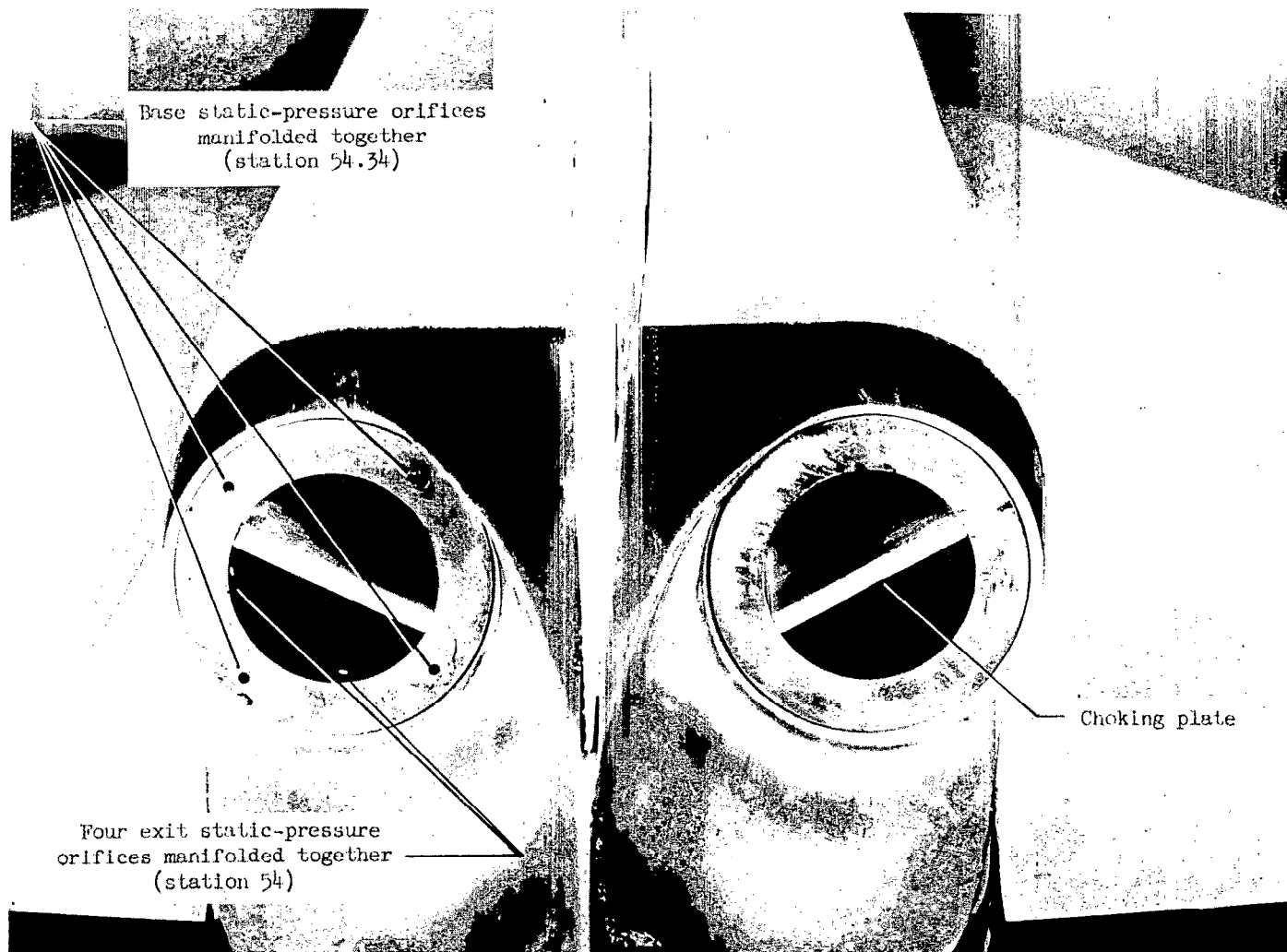
Choking plate

L-83894.1

Figure 6.- Aft end of model showing locations of static-pressure orifices
and choking plates in exits.
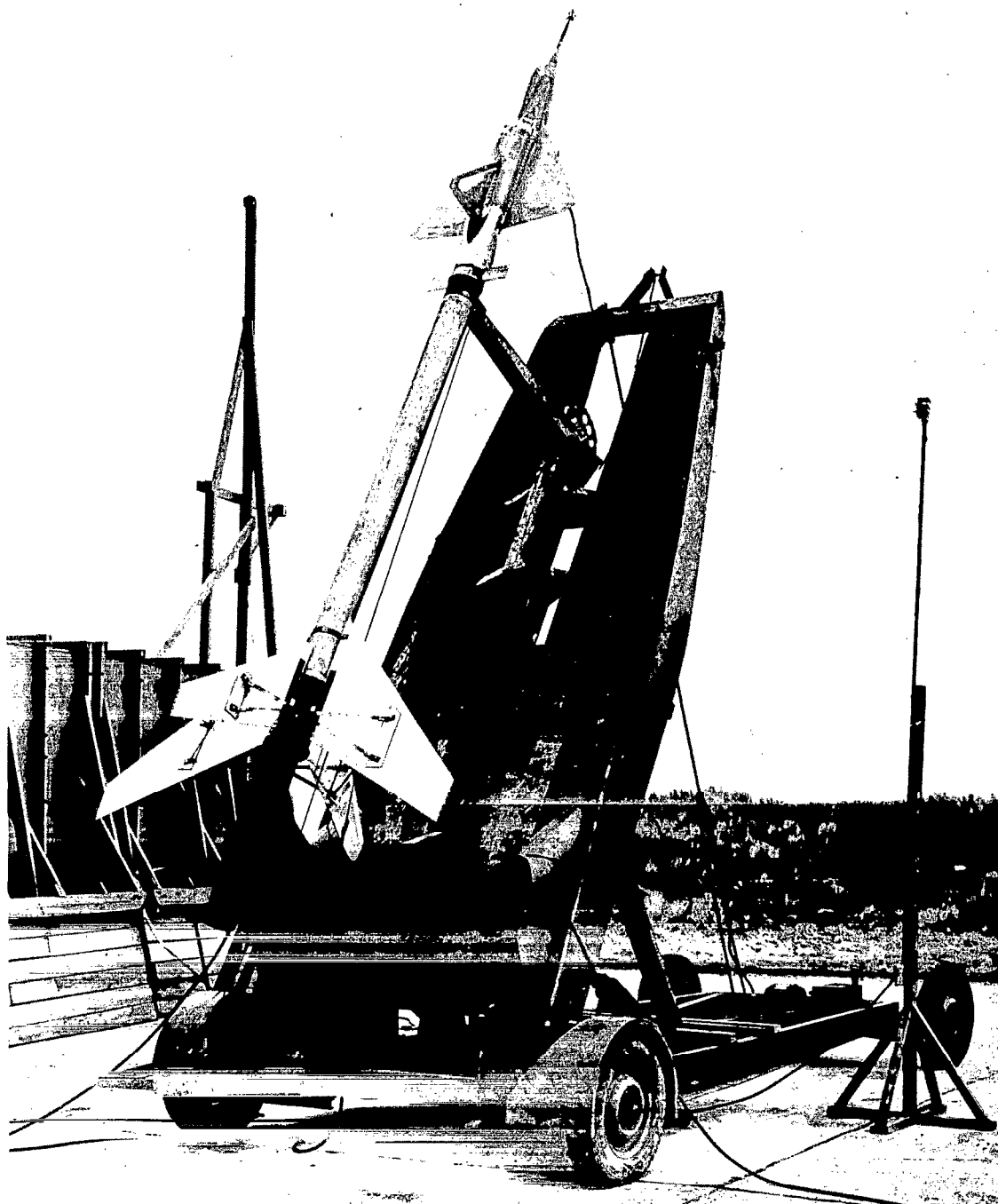
L-84153.1

Figure 7.- Model and booster assembly on mobile launcher.
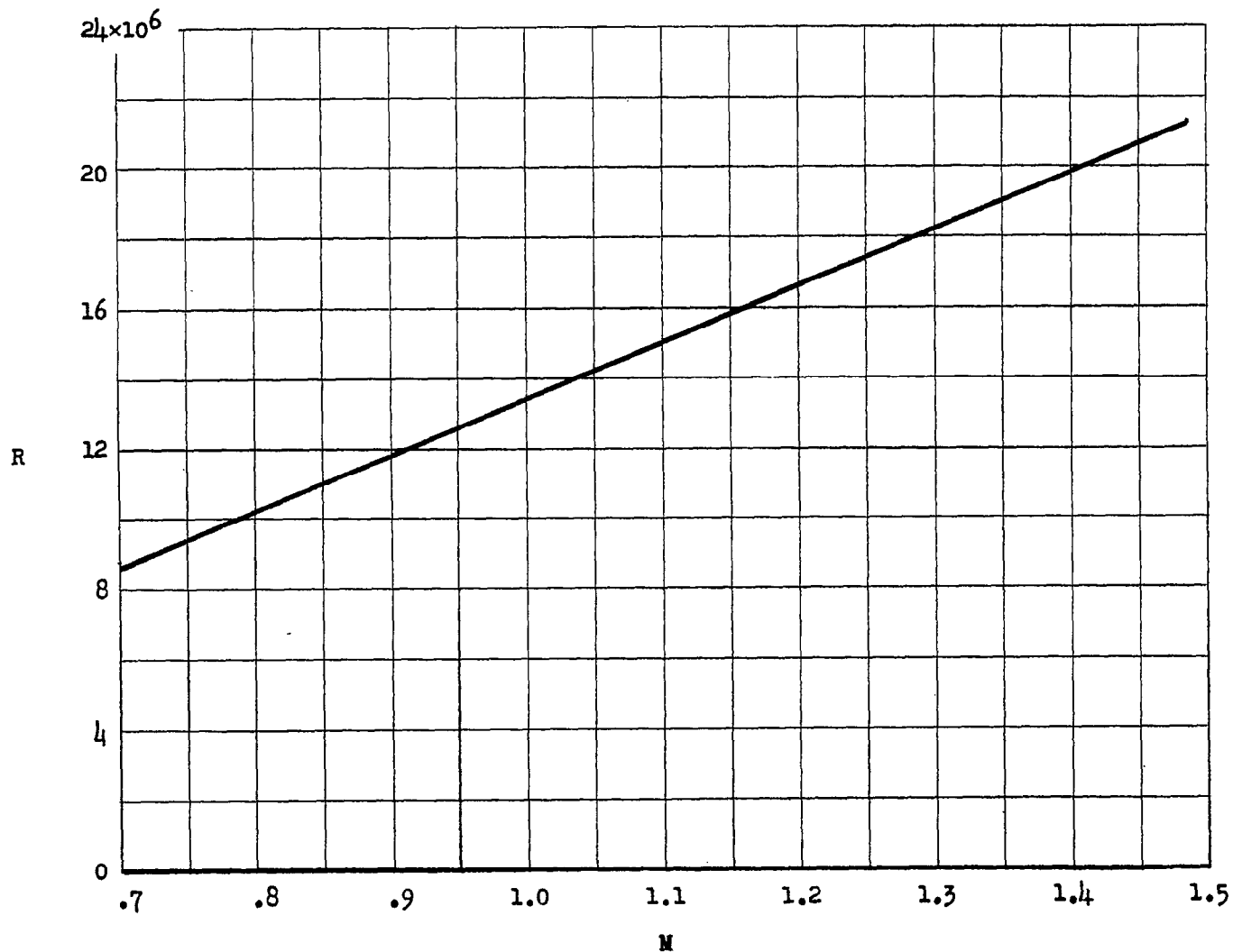
Figure 8.- Variation of Reynolds number, based on the mean aerodynamic chord, with Mach number.
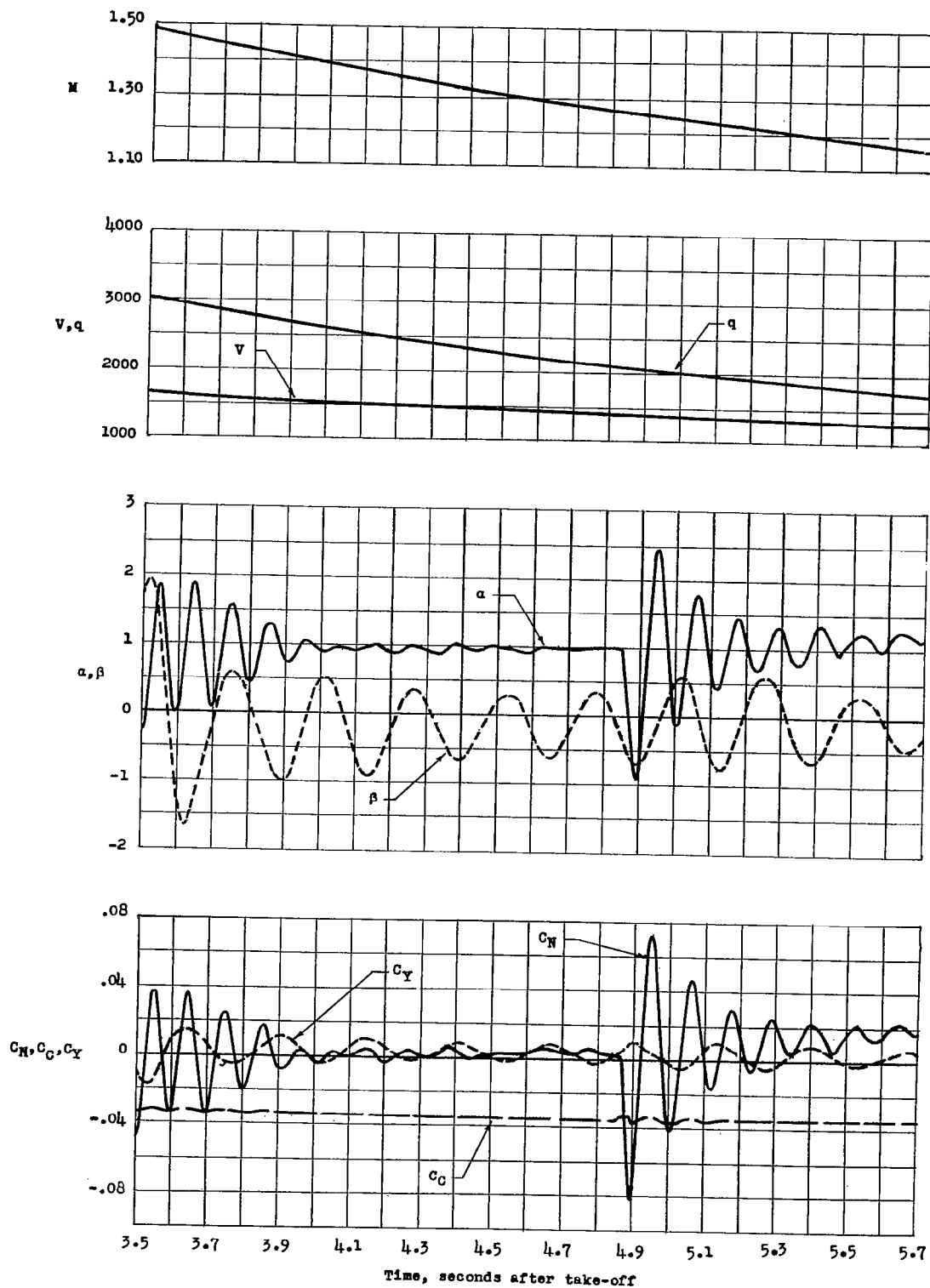
Figure 9.- Samples of time histories of some of the quantities obtained.
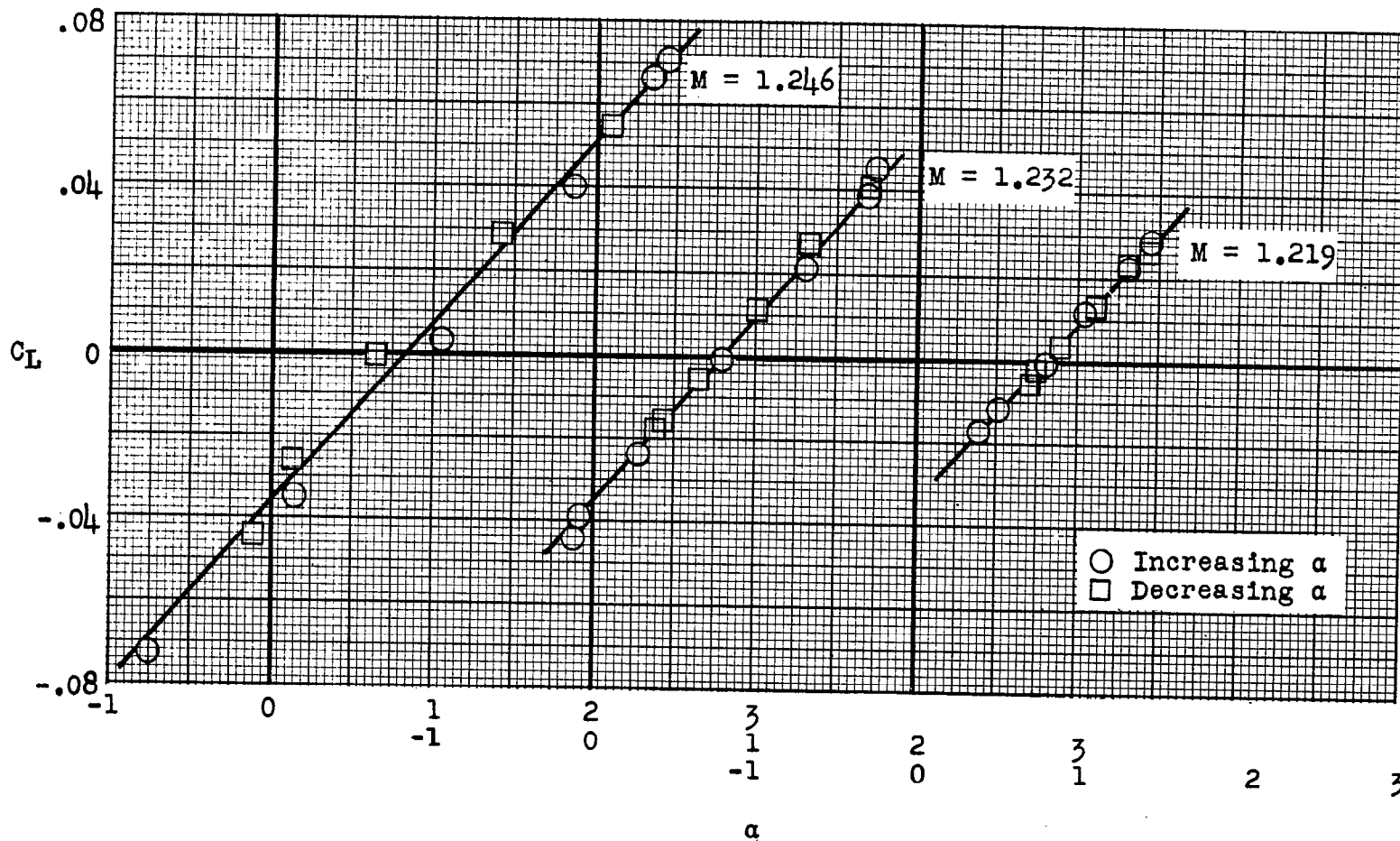
Figure 10.- Typical variation of lift coefficient with angle of attack.
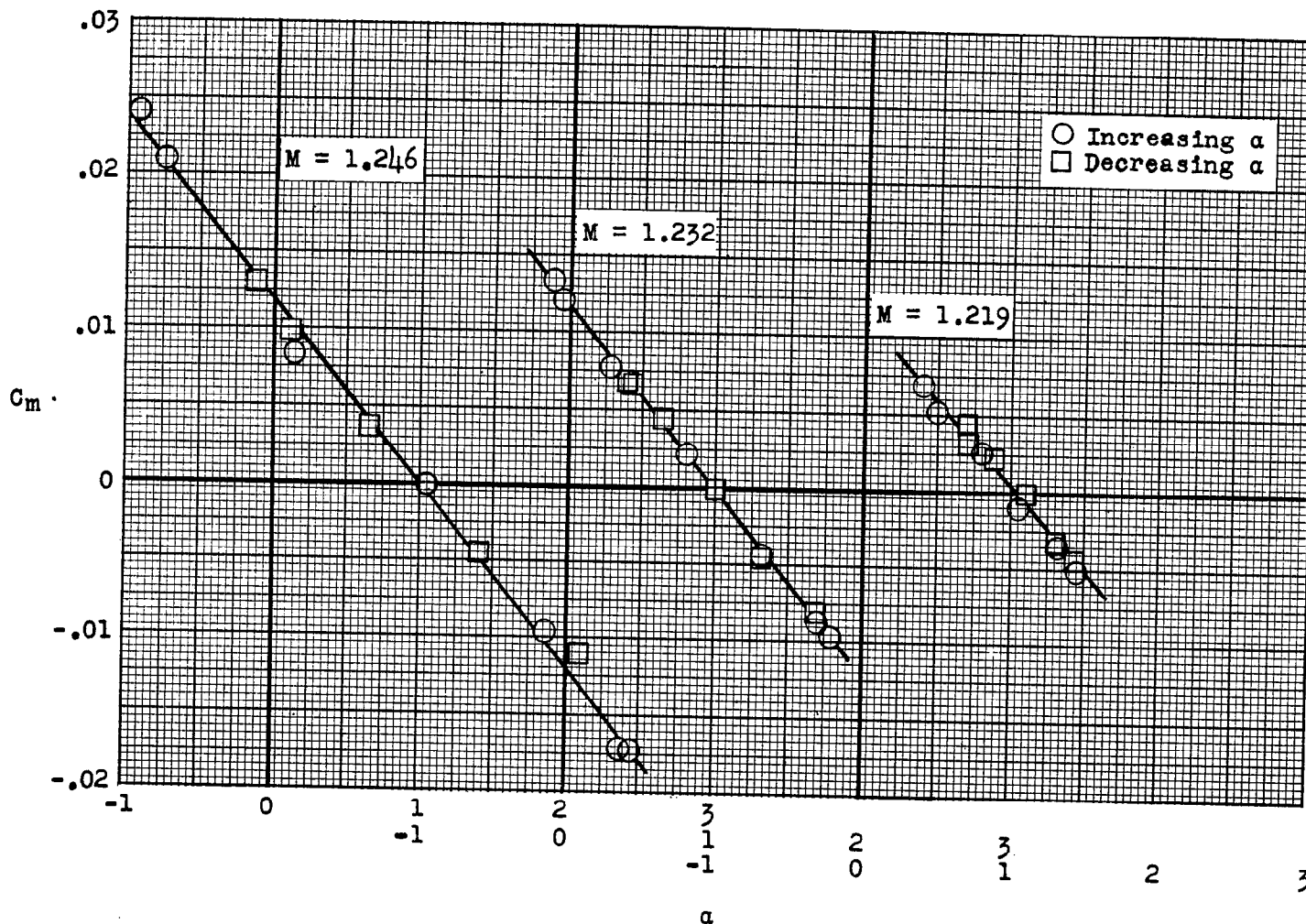
Figure 11.- Typical variation of total pitching-moment coefficient with angle of attack. Center of gravity at 19.52 percent mean aerodynamic chord.
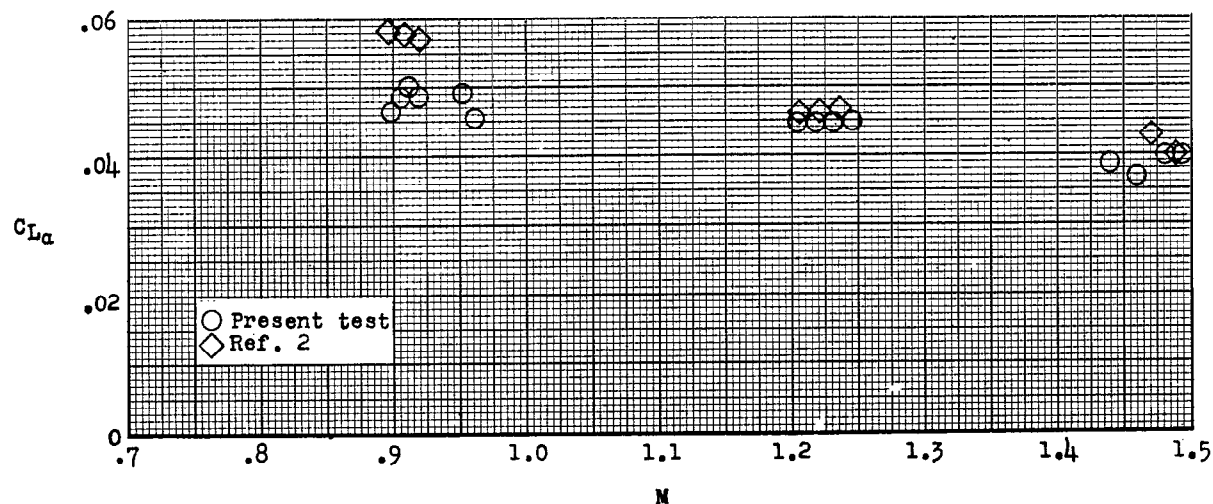
(a) Slope of lift curve.
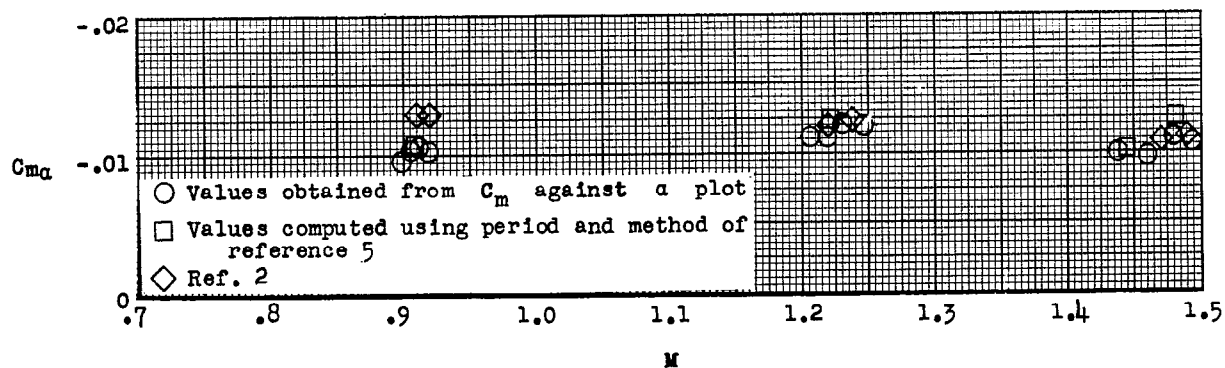
(b) Static-longitudinal-stability derivative.

Figure 12.- The variations with Mach number of the longitudinal-
stability parameters.
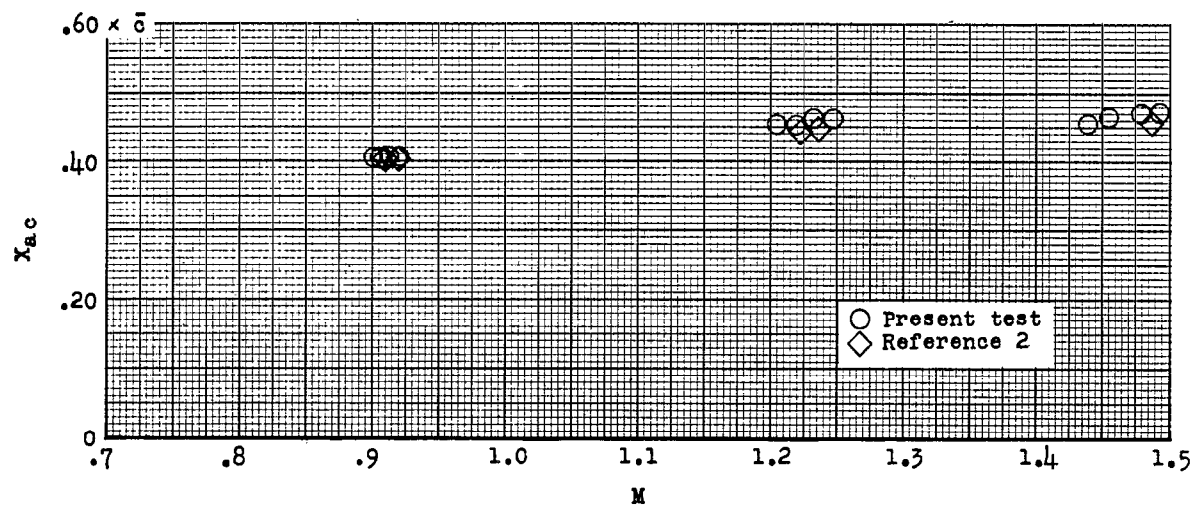
(c) Aerodynamic-center location.
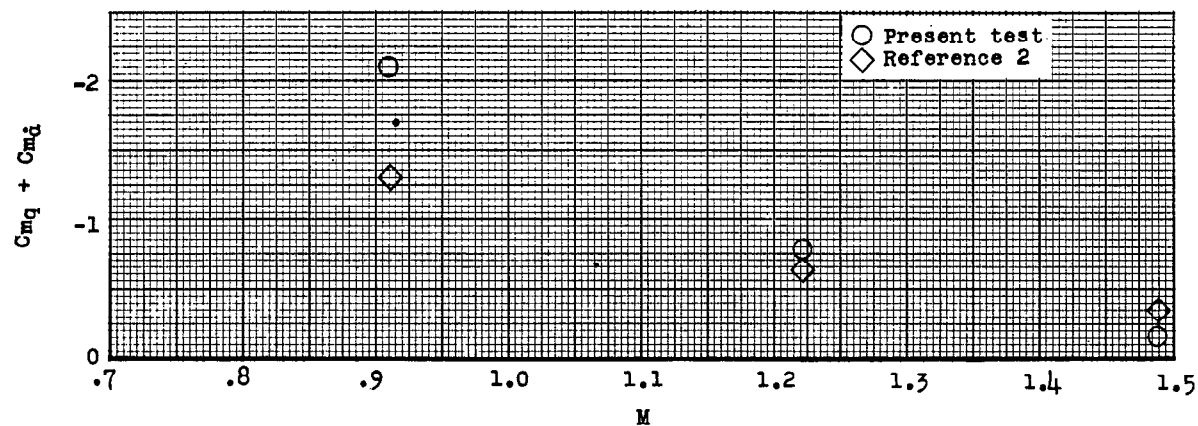
(d) Damping-in-pitch derivatives.

Figure 12.- Concluded.
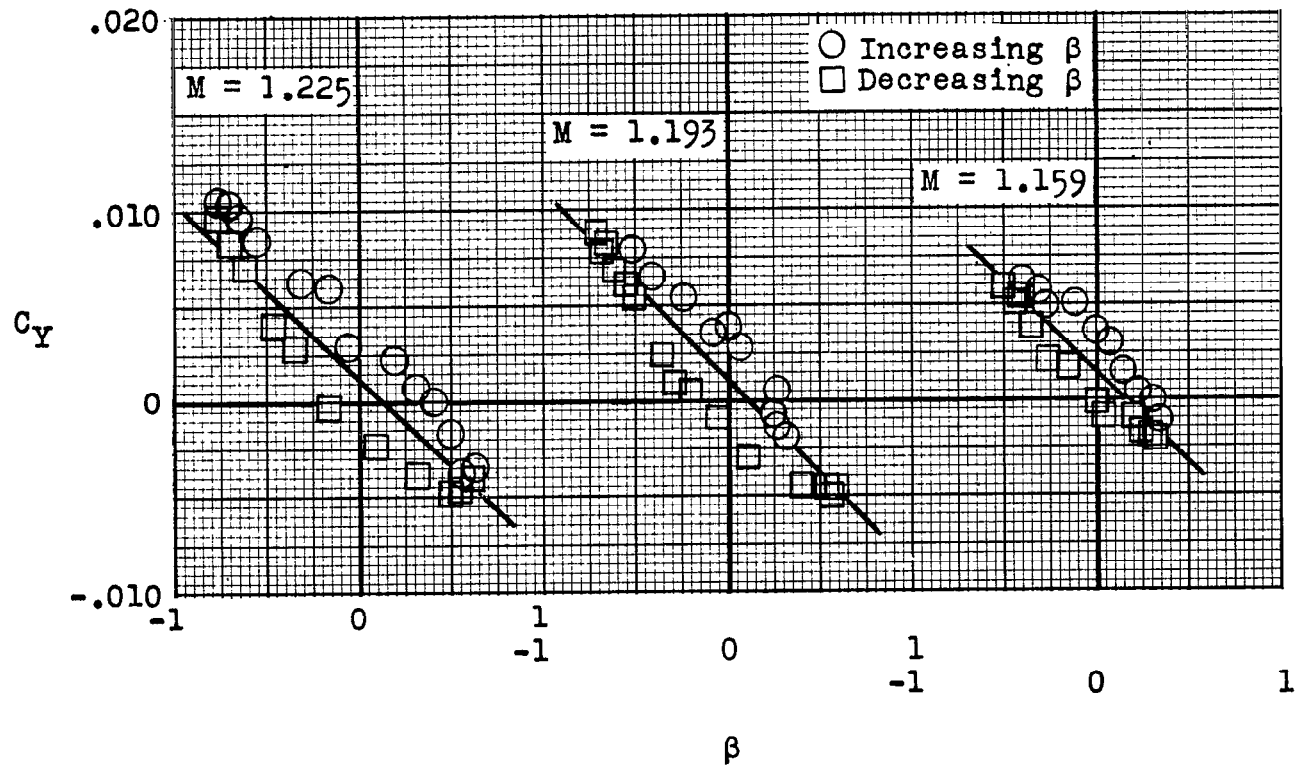
Figure 13.- Typical variations of side-force coefficient with angle of
sideslip.
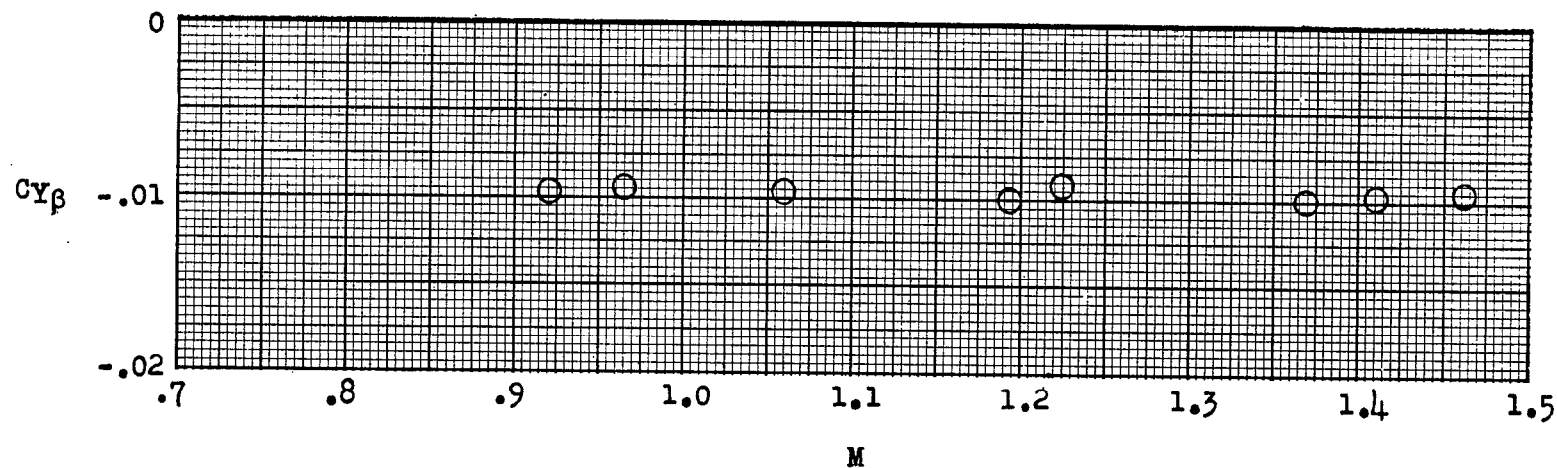
Figure 14.- Variation of slope of side-force coefficient with Mach number.
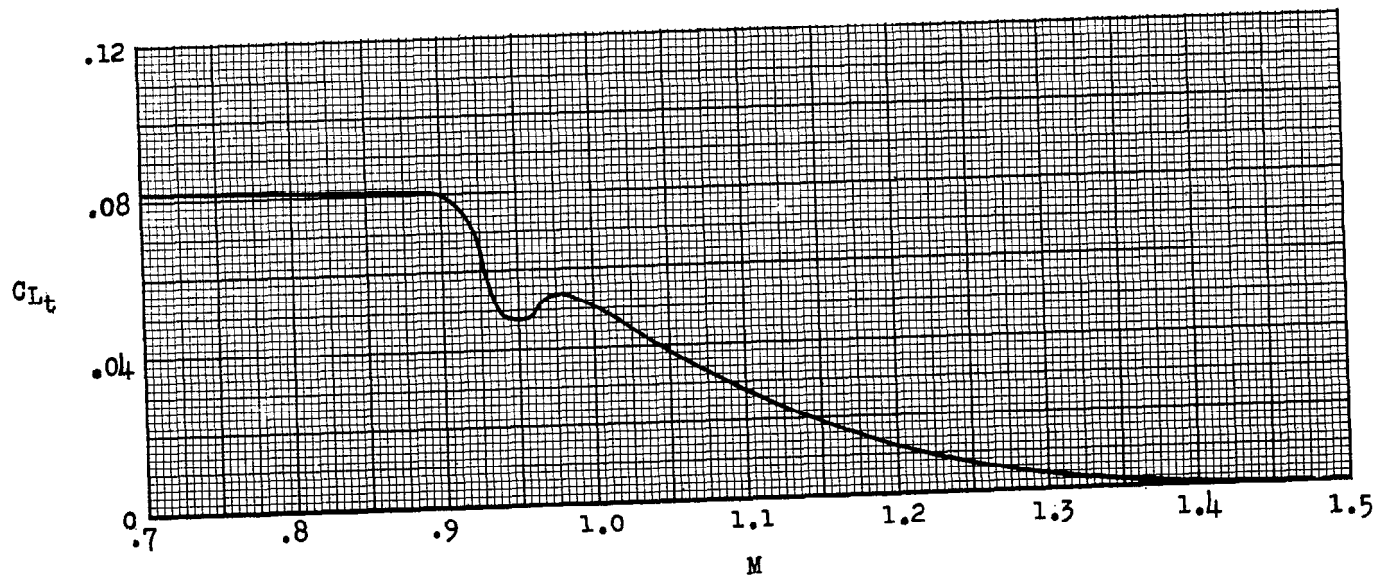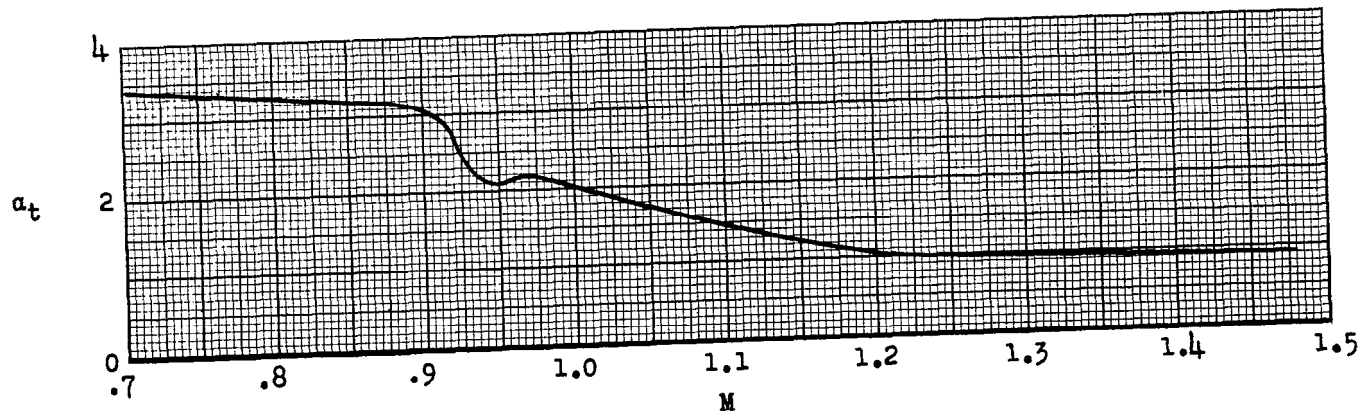
Figure 15.- The variation with Mach number of the trim angle of attack and the trim lift coefficient.
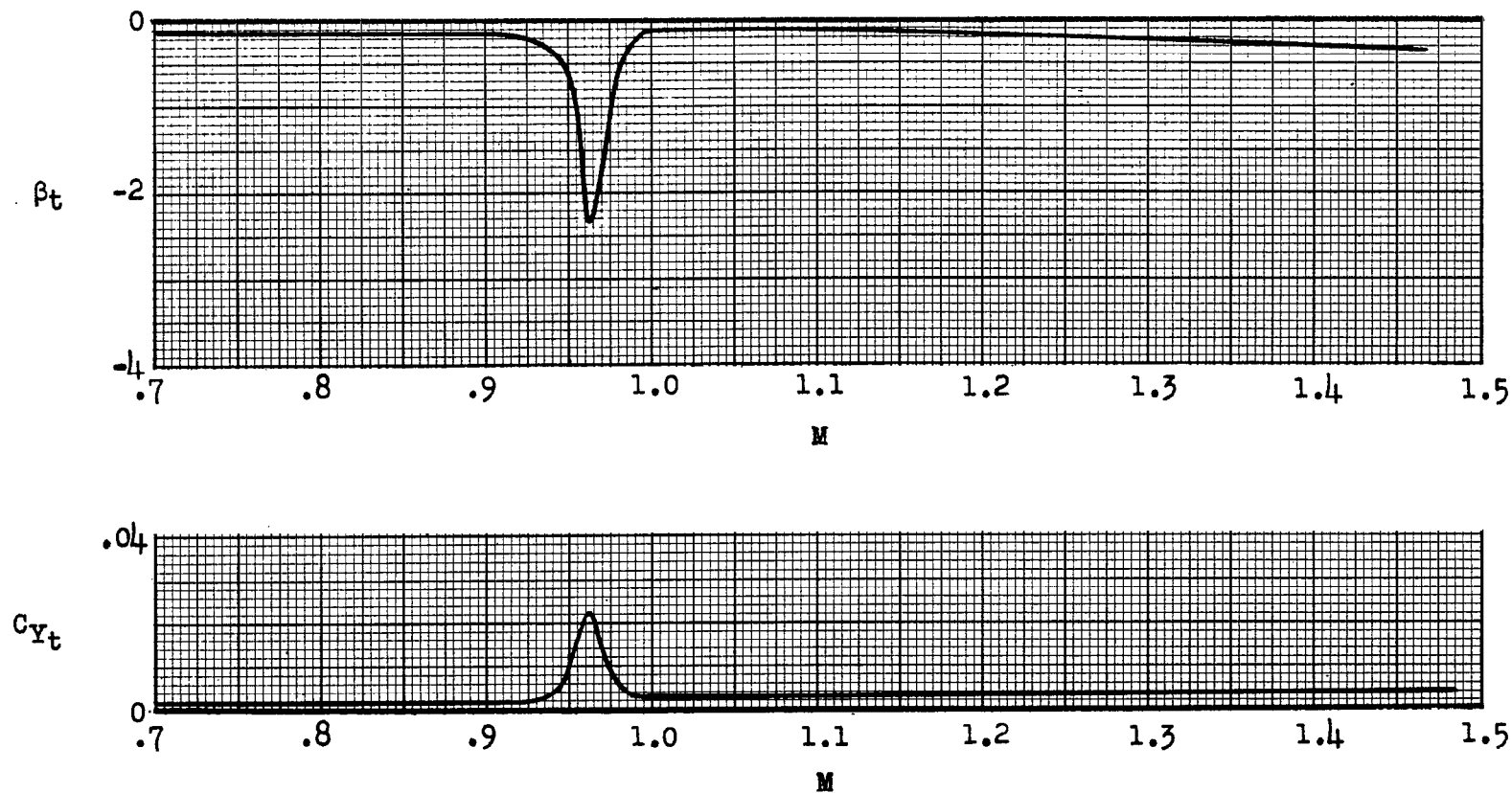
Figure 16.- The variation with Mach number of the trim angle of sideslip
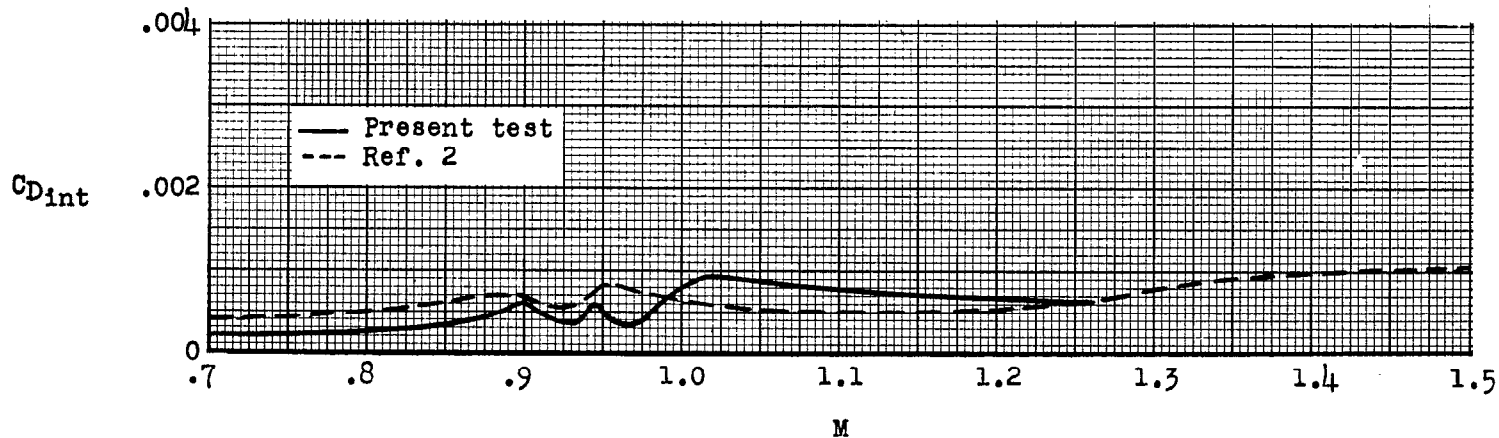and the trim side-force coefficient.
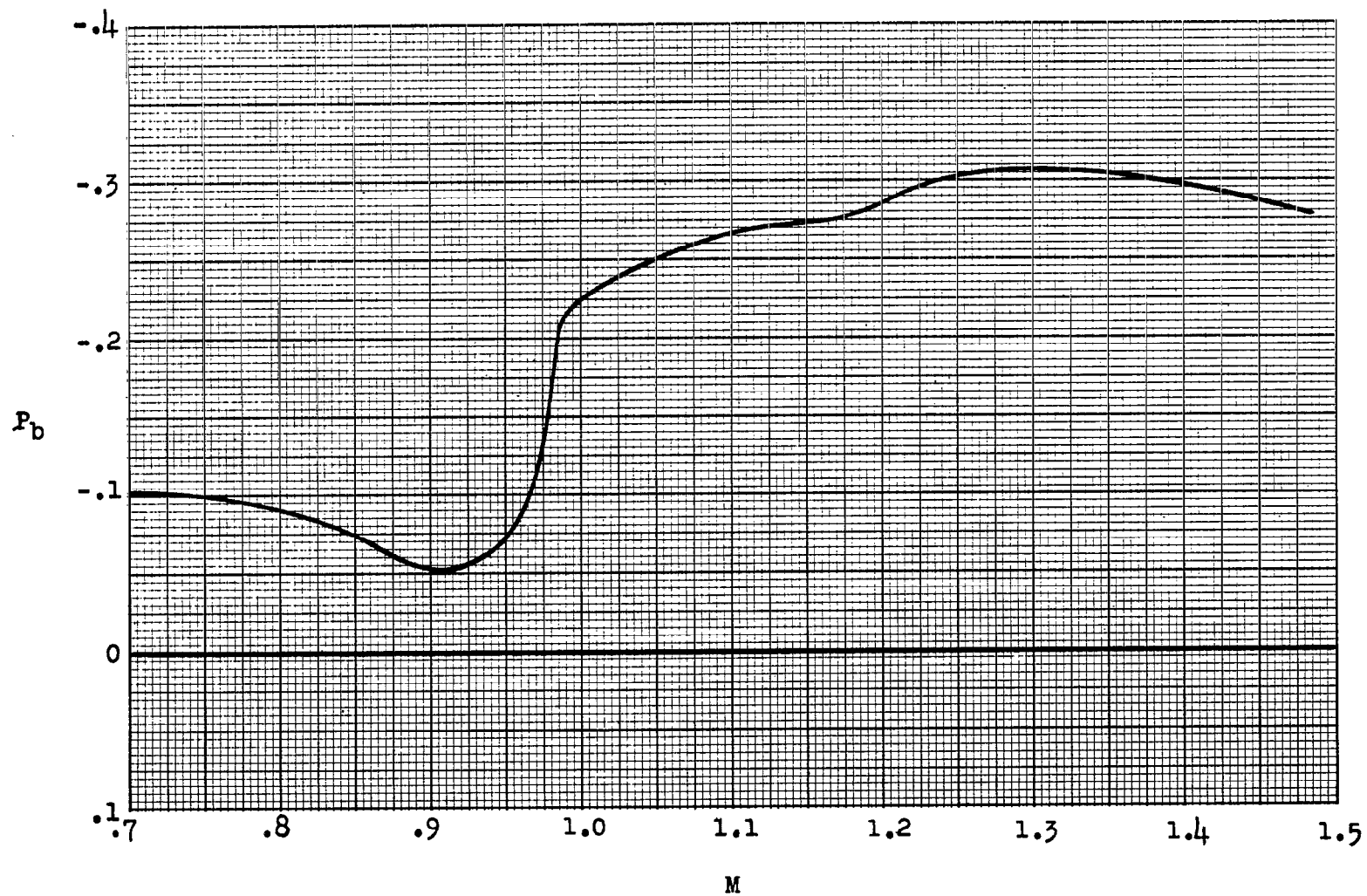
Figure 17.- Variation of base pressure coefficient with Mach number.
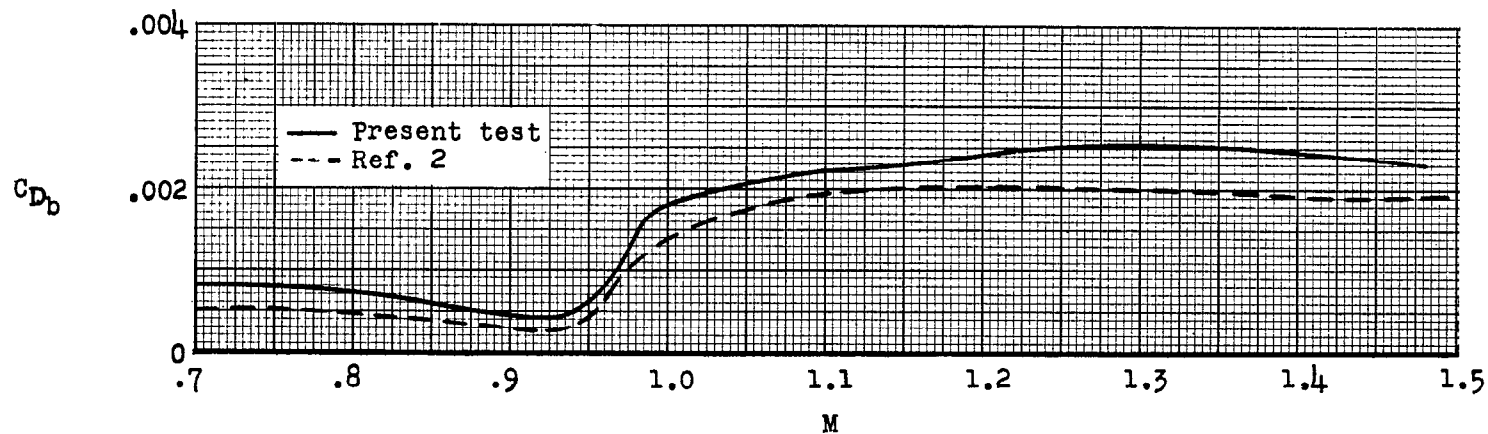
(a) Base drag coefficient.

(b) Internal-drag coefficient.

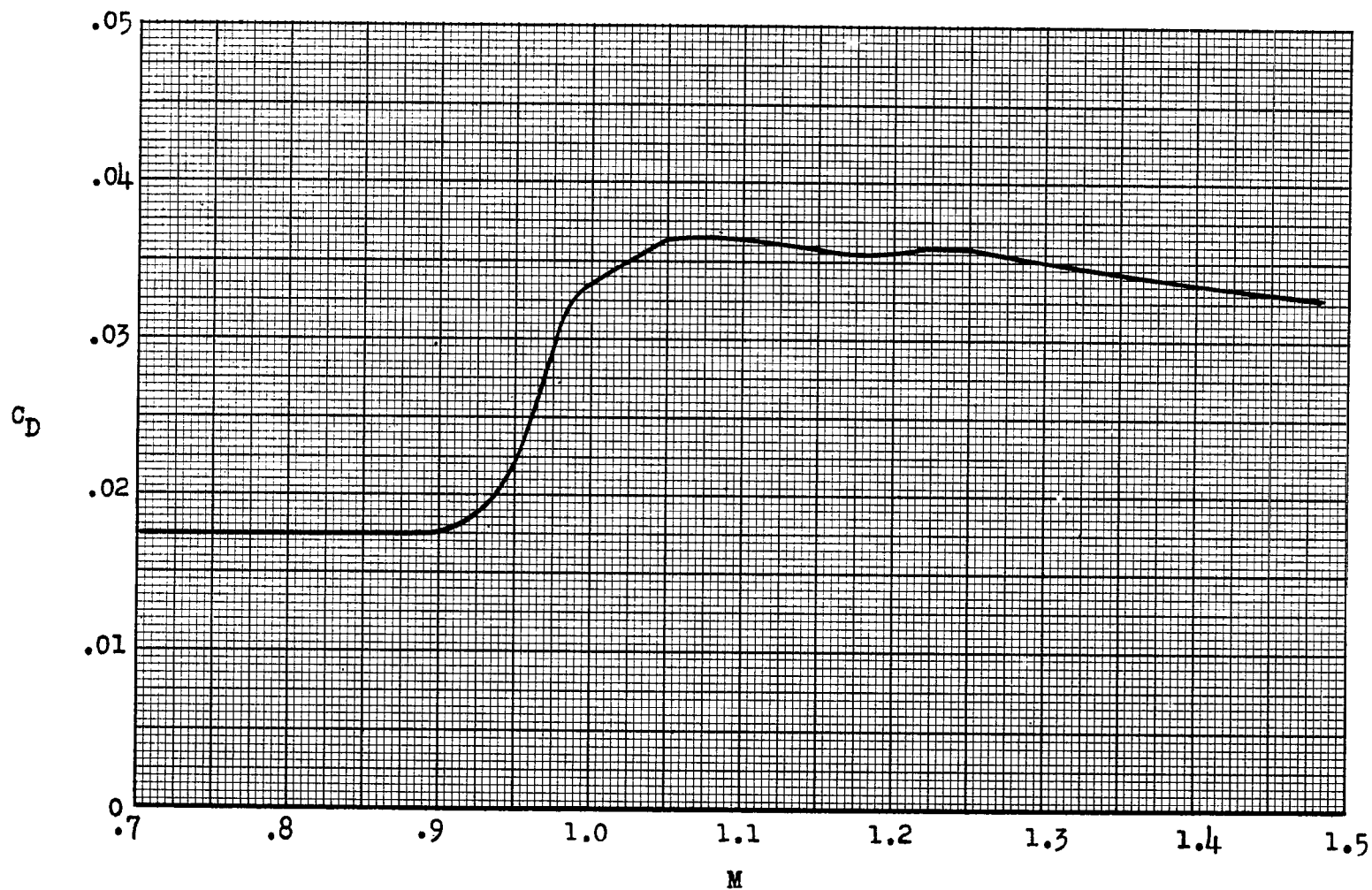Figure 18.- Variation of some drag-coefficient components with Mach number.

Figure 19.- The variation of the total drag coefficient with Mach number for the trim conditions of the test.
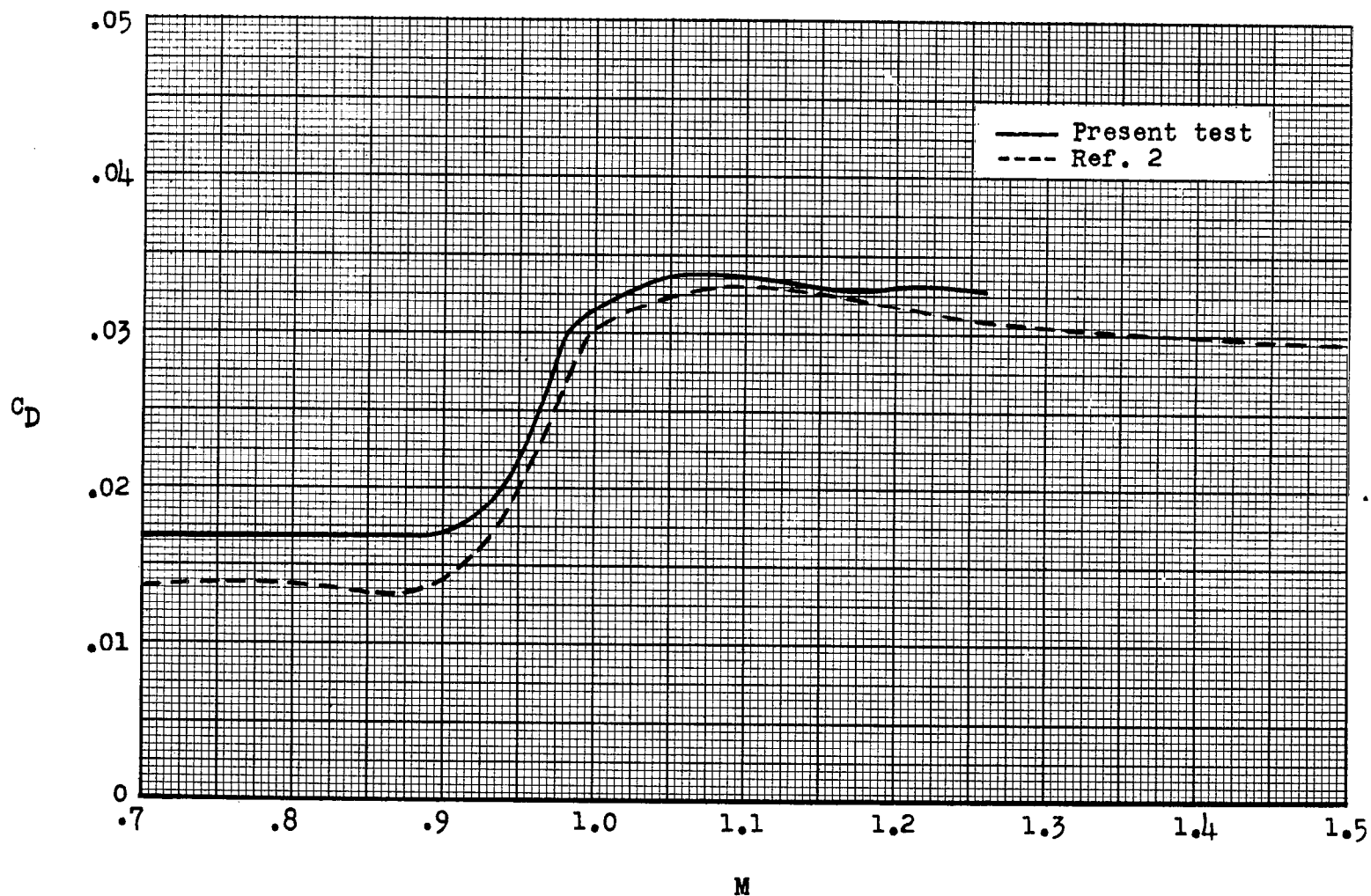
Figure 20.- The variation of the net drag coefficient with Mach number for the trim conditions of the respective test.
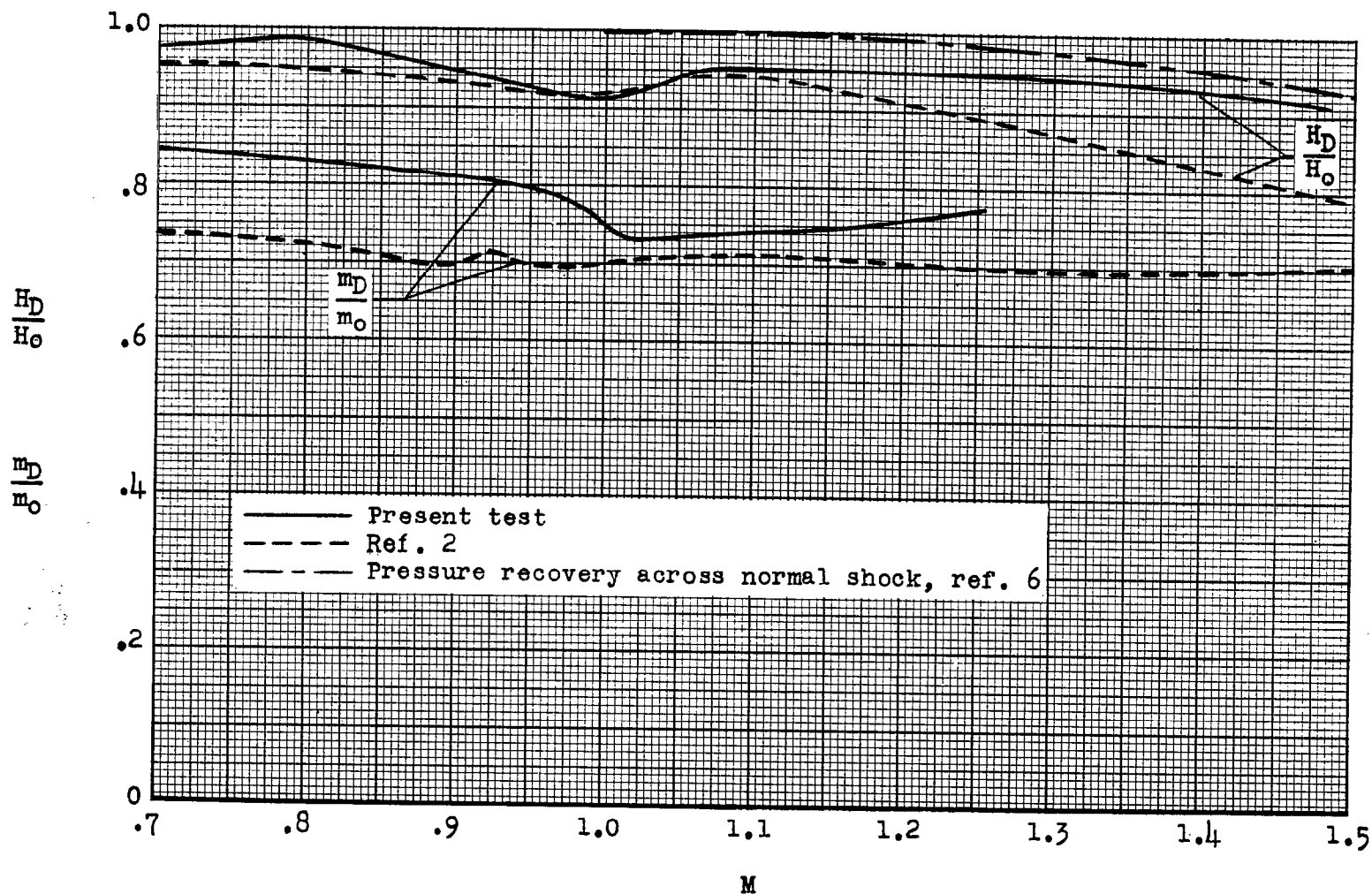
Figure 21.- Variation with Mach number of the total-pressure ratio at
compressor-face location and the mass-flow ratio at the duct exit.